J Electr Eng Technol.2018; 13(4): 1644-1654
http://doi.org/10.5370/JEET.2018.13.4.1644

ISSN(Print) 1975-0102
ISSN(Online) 2093-7423

Modal Analysis of Point and Discretized Continuous Spectra for Metal-Insulator-Metal Waveguides in the Terahertz Region

Jun Hur*, Hosung Choo* and Jong-Eon Park†

Abstract – Eigenvalue distributions for a periodic metal-insulator-metal waveguide, classified into the point spectrum and the discretized continuous spectrum (DCS), are investigated as functions of frequencies, gap widths, and periods. Muller's method is suggested for solving exact eigenvalues, and we propose the scheme for finding proper initial values in the Muller's method by considering only $\Re\mathfrak{e}(\varepsilon_r)$ in the dispersion equation. We then find that anti-crossing behavior, repulsive effect between the point spectrum and the DCS, becomes stronger when the real parts of the roots in the point spectrum have smaller values. Finally, we examine the transmittances of a single subwavelength slit for real metals using the mode matching technique. The transmittances in real metals similarly follow those of the perfect electric conductor (PEC) at low frequencies, while the patterns at higher frequencies begin to differ from the PEC.

Keywords: Metal-insulator-metal waveguide, Muller's method, Anti-crossing behavior, Mode matching technique, Transmittance

1. Introduction

Researches on the transmission of electromagnetic waves through slits or apertures in terahertz (THz) frequencies have been recently investigated [1-7]. The fundamental guided geometry with one-dimensional metal-insulator-metal (MIM) layer is known as the metal-insulator-metal waveguide (MIMW). The MIMW becomes more important in THz applications, especially in guiding structures or subwavelength apertures, to study the reflection and transmission effects of discontinuities and their multi-junction structures. To explain the basic concept of the MIMW, it is necessary to understand the transition from dielectric slab waveguides (DSWs) to parallel plate waveguides (PPWs). The relative permittivity of metals can be written as:

$$\varepsilon_r = \varepsilon' - j\varepsilon''. \tag{1}$$

The real parts of the permittivities $\Re\mathfrak{e}(\varepsilon_r)$ in real metals, such as gold, silver, aluminum, and copper, are usually negative quantities in the THz regime below the plasma frequency [8] as well as microwave frequencies. As the frequency decreases and approaches the microwave band, the $|\Re\mathfrak{e}(\varepsilon_r)|$ increases as listed in Table 1. Moreover, the $|\Im\mathfrak{m}(\varepsilon_r)|$ grows drastically to $|\Im\mathfrak{m}(\varepsilon_r)| >> |\Re\mathfrak{e}(\varepsilon_r)|$ in the frequency range below 10 THz, and this abrupt increase in $|\Im\mathfrak{m}(\varepsilon_r)|$ is due to not only the damping loss by molecules but also the conductivity of real metals. The conducting effect predominates over the microwave band and then the metal can be regarded as a perfect electric conductor (PEC). In such a case, the electromagnetic field inside the PEC is zero, and the MIMW can be regarded as the PPW. On the other hand, $\Re\mathfrak{e}(\varepsilon_r)$ of real metals in frequency range of near-infrared or visible light has a negative value, and $|\Im\mathfrak{m}(\varepsilon_r)|$ is getting smaller than that in the microwave band, resulting in $|\Im\mathfrak{m}(\varepsilon_r)| < |\Re\mathfrak{e}(\varepsilon_r)|$. In this case, the $\Im\mathfrak{m}(\varepsilon_r)$ mostly stands for the damping loss, and the electromagnetic waves can penetrate the real metals due to the small $|\Im\mathfrak{m}(\varepsilon_r)|$. Assuming that the loss by $\Im\mathfrak{m}(\varepsilon_r)$ is extremely small enough to be ignored, the MIMW can be approximated to the DSW.

Modal analysis [9, 10] is the most fundamental and intuitive method to investigate the electromagnetic behaviors in the MIMW and the transition characteristics between PPW and DSW. The eigenvalues in the MIMW are separated into the point and continuous spectra [4, 11, 12]. The point spectrum is reclassified into the

Table 1. Relative permittivities $\varepsilon_{r,m}$ of Ag, Cu, and Al [18].

Frequency (THz)	Ag	Cu	Al
1.2	−192760 − *j*731720	−13536 − *j*158760	−44623 − *j*513470
10	−37433 − *j*21558	−7032.0 − *j*15057	−30276 − *j*33929
30	−3738.3 − *j*1487.3	−4030.1 − *j*1090.7	−6361.9 − *j*3670.2
50	−1470.8 − *j*355.65	−1509.2 − *j*288.09	−2776.2 − *j*1294.0
100	−380.76 − *j*48.957	−389.12 − *j*59.843	−845.11 − *j*245.75
200	−94.108 − *j*7.567	−100.72 − *j*14.034	−213.96 − *j*42.987

† Corresponding Author: Metamaterial Electronic Device Research Center, Hongik University, Korea. (jongeon.park@gmail.com)
* School of Electronic and Electrical Engineering, Hongik University, Korea. (gjwns0@naver.com, hschoo@hongik.ac.kr)
Received: December 4, 2017; Accepted: February 6, 2018

propagating, evanescent, and anomalous modes [1] similar to the spectrum of the PPW, except the anomalous one. The point spectrum can explain the sinusoidal electromagnetic field patterns in the insulator. In the MIMW, the eigenvalues of the continuous spectrum are discretized and is renamed to the discretized continuous spectrum (DCS) [4]. The DCS describes the sinusoidal field patterns mainly in the metal region and imitates the radiation mode in DSW, but there is no role for radiation. From the eigenvalues of the spectra, the electromagnetic field patterns, propagating properties, and orthogonal relation among modes can be explained in detail.

The theories of the modal analyses and their completeness for the DSW and PPW are well established, but recently MIMWs has been studied and their relevant literature has been published [1, 2, 4]. Propagating and evanescent modes depending on various relative permittivities, boundaries between evanescent and anomalous eigenvalues according to the gap width, and confluence of anomalous modes for MIMW are discussed [1]. The modal analysis for the waveguides, their field patterns, backward and forward modes for each eigenvalue, and completeness are also described in detail and are verified using finite-difference frequency-domain (FDFD) method [4]. Transmission and scattering properties of subwavelength slits in metals are dealt in [5]. Imaginary metals being arbitrarily suggested with negative $\Re e(\varepsilon_r)$ are applied in the subwavelength slit geometries and compared with PEC in terms of transmission efficiencies [6]. The study on the MIMW is extended to the characteristic observation of the transmittances of deep-subwavelength slit at THz frequencies [7]. However, the relative permittivity of a particular wavelength for silver [4] and limited range of frequencies [1-6] are observed in the previous studies. In addition, the analysis of eigenvalues and their distributions are not fully investigated in detail.

In this paper, we examine the distribution of eigenvalues of MIMW at THz frequencies. In particular, we analyze the eigenvalues of the point spectrum and DCS for real metals in accordance with frequencies, gap widths, and periods of MIMW. First, several preliminaries, such as the basic geometry of MIMW and material properties of real metals are introduced. The dispersion equation in MIMW is presented, and then the Muller's method [13] rather than the others is adopted to solve the dispersion equation. The Muller's method is especially robust for finding the complex solutions when proper initial roots are given. Since the large amount of $|\Im m(\varepsilon_r)|$ makes one difficult to find eigenvalue solutions in the Muller's method, we propose the scheme for finding proper initial values of the dispersion equation by considering only $\Re e(\varepsilon_r)$, and then the exact roots can be iteratively found by increasing the imaginary part $|\Im m(\varepsilon_r)|$ in the Muller's method.

Next, the distributions of the spectra as a function of frequency are investigated. As the frequency (or wavelength) varies, the relative permittivity changes as well, so the solution also varies significantly. We observe the eigenvalue distributions of both the point spectrum and DCS for various subwavelength slit widths and periods. The anti-crossing behavior which seems to be inherent to satisfy the orthogonality among the modes will be explained. Finally, by applying the point spectrum and DCS to mode matching technique (MMT), the transmittances through the subwavelength slit in real metals are obtained and compared to the results using the subwavelength slit in PEC. The transmission characteristics can be applied to the optical applications such as the optical bend, splitter, switch, and demultiplexer [14, 15].

2. Preliminaries

2.1 Problem geometry and dispersion equation

Figs. 1(a) and 1(b) describe the geometry of the MIMW to be analyzed. An electromagnetic wave with TM modes propagates along z-axis. The structure has a period of $2(g+h)$ in the x-axis, where the thicknesses of the metal and the insulator are $2h$ and $2g$, respectively, and it is uniform along the y-axis. The waveguide structure is composed of layers arranged in the order of metal, insulator, and metal,

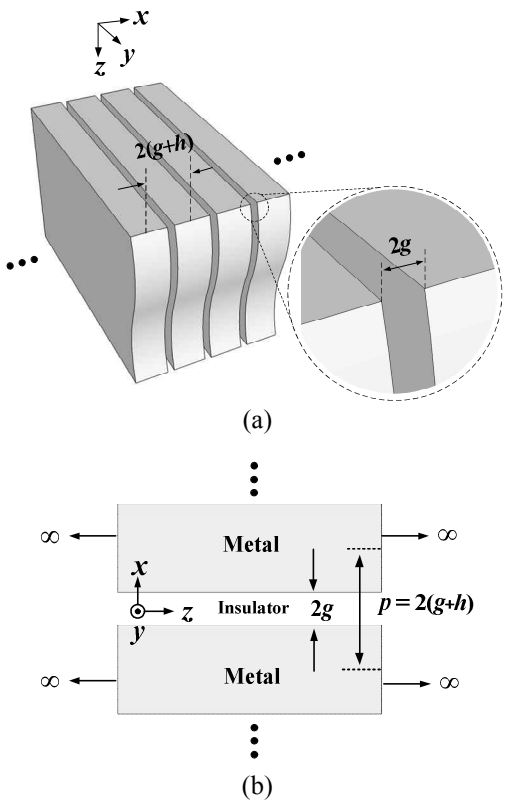

Fig. 1 Geometry of the periodic MIMW with the gap width $2g$ and the period $2(g+h)$. (a) Perspective view. (b) Side view. The MIMW is one-dimensional structure which is independent of y and z directions

and is thus called MIM waveguide (MIMW). In this paper, an insulator is fixed to vacuum ($\varepsilon_{r,i}$ = 1). The operation principle of the MIMW is similar to the DSW that usually comprises the vacuum-dielectric-vacuum layers, because the arrangement of relative permittivities in MIMW and DSW are comparable to each other. Small ($g < x < g+h$), large ($-g \le x \le g$), and small ($-g-h < x < -g$) permittivities in both guide structures allow electromagnetic waves to propagate mainly along the central material ($-g \le x \le g$). We will consider only even modes because the even modes are enough to discuss the normal incidence for the MIMW. Both even and odd modes can be dealt with in the case of oblique incidence plane waves, which is beyond the scope of our work. The dispersion equation, the most fundamental equation in the MIMW, by assuming $e^{+j\omega t}$ time convention, is obtained as follows [1, 4, 16, 17]:

$$\tanh\left(\kappa_{i,n} g\right) = -\frac{\kappa_{m,n} / \varepsilon_{r,m}}{\kappa_{i,n} / \varepsilon_{r,i}} \tanh\left(\kappa_{m,n} h\right) \tag{2}$$

, where $k_{z,n}^2 = \kappa_{m,n}^2 + \omega^2 \mu \varepsilon_{r,m} = \kappa_{i,n}^2 + \omega^2 \mu \varepsilon_{r,i}$. (3)

$\varepsilon_{r,m}$ and $\varepsilon_{r,i}$ are relative permittivities in metal and insulator, respectively. $\kappa_{m,n}$ and $\kappa_{i,n}$ are n^{th} transverse propagation constants in metal and insulator, respectively, and $k_{z,n}$ is the n^{th} propagation constant along z-axis. The subscripts n in $\kappa_{m,n}$, $\kappa_{i,n}$, and $k_{z,n}$ commonly indicate the n^{th} modes, which are related to one another as in Eq. (3). The roots $\{\kappa_{m,n}\}$s of the dispersion equation are found using Muller's method while varying the geometrical parameters (g and h) as well as the material parameter ($\varepsilon_{r,m}$).

2.2 Material properties of real metals at THz frequencies

For reference, the relative permittivities of a number of metals at several THz frequencies are listed in Table 1 [18]. The imaginary parts of relative permittivities are given as negative numbers. As the frequency decreases, the magnitudes of both real and imaginary parts are increased. The material properties in Table 1 are applied in Eq. (2) and later in Section 3.

2.3 Muller's method

There are well-known and classical numerical roots finding methods, such as the bisection method, Newton's method, and secant method. However, these numerical techniques are limited to the equations with real-valued roots. The Muller's method is effective in obtaining not only real, but also complex roots of arbitrary functions $f(x)$ = 0 [13]. Even if there is the argument principle method [19], which is one of the other well-known ways of solving complex roots, the Muller's method is more accurate and easier to obtain solutions once approximate roots are given. Therefore, only the Muller's method is applied to solve the eigenvalues for the dispersion equation throughout the next section. Other complex root-finding methods can be found in [20-22].

2.4 Point spectrum and discretized continuous spectrum

The dispersion equation of the *non-periodic* MIMW with the gap width 2g can be easily derived by increasing h to ∞ in Eq. (2). The geometry is comprised of metal ($-\infty < x < -g$), insulator ($-g \le x \le g$), and metal ($g < x < \infty$). Then, the eigenvalues in Eq. (2) can be classified into point and continuous spectra [4]. The point spectrum can be again categorized into propagating, evanescent, and anomalous modes. The point spectrum predominantly describes the H-field patterns in the *insulator* as sinusoidal harmonics, while the continuous spectrum mainly expresses the field patterns in the *metal*. However, when the non-periodic structure is changed into a periodic structure, the continuous spectrum is discretized and is again referred to as the DCS. To solve the transmittance through a subwavelength slit, it is much easier to deal with the DCS rather than the continuous spectrum in numerical calculations. Therefore, we investigate the DCS, not the continuous spectrum, with the point spectrum in the next sections.

3. Analysis of Point and Discretized Continuous Spectra

In this section, we investigate the point spectrum and DCS distributions as functions of frequencies, gap widths, and periods. Only aluminum is taken into account as the material property of the real metal in Section 3.

3.1 Scheme for finding roots in the point spectrum

The Muller's method is especially robust for finding the complex roots when initial approximate roots are given. Since a large amount of $|\Im\mathfrak{m}(\varepsilon_{r,m})|$ makes one difficult to find eigenvalue solutions in the Muller's method, we propose the scheme for finding proper initial values of the dispersion equation by considering only $\Re\mathfrak{e}(\varepsilon_{r,m})$, and then the exact roots can be iteratively found by gradually increasing the imaginary part $|\Im\mathfrak{m}(\varepsilon_{r,m})|$ in the Muller's method. If too large or entire value of $\Im\mathfrak{m}(\varepsilon_{r,m})$ is used in the Muller's method, the resulting root can lead to an incorrect solution. The detailed procedure for finding roots is as follows: (i) Although the exact $\varepsilon_{r,m}$ is a complex number as listed in Table 1, if we consider only the real part of $\varepsilon_{r,m}$, we can efficiently find the proper initial roots in the point spectrum. By substituting Eq. (3) into Eq. (2), $\kappa_{i,n}$ can be eliminated, and Eq. (2) is rearranged as

$$f(x)=\tanh\left(\sqrt{x^2+\varepsilon_{r,m}-\varepsilon_{r,i}}\times(k_0 g)\right)+\frac{\varepsilon_{r,i}}{\varepsilon_{r,m}}\frac{x}{\sqrt{x^2+\varepsilon_{r,m}-\varepsilon_{r,i}}}\tanh\left(x\times(k_0 h)\right)=0. \quad (4)$$

x is normalized transverse propagation constant $\kappa_{m,n}/k_0$ to be solved, and k_0 is free-space wavenumber. Once we find the first root $\kappa_{m,0}/k_0$, then $\kappa_{i,0}/k_0$ and $k_{z,0}$ are obtained by Eq. (3). The subscript 0s in $\kappa_{m,0}$, $\kappa_{i,0}$, and $k_{z,0}$ indicate the TM_0 mode in MIMW and the first root in the point spectrum. TM_2, TM_4, etc. are the next even modes, and TM_1, TM_3, etc. are ignored since the odd modes are ruled out. If we set the insulator in a MIMW as vacuum, $\varepsilon_{r,i}$ = 1, then Eq. (4) can be arranged as

$$\frac{x}{\sqrt{x^2+\varepsilon_{r,m}-1}}\times\frac{\tanh\left(x\times(k_0 h)\right)}{\tanh\left(\sqrt{x^2+\varepsilon_{r,m}-1}\times(k_0 g)\right)}=-\varepsilon_{r,m}. \quad (5)$$

where $\varepsilon_{r,m}$ is purely real, and thus the Eq. (5) can be solved relatively easily, and the first root should be found in vicinity of $x=\sqrt{-\varepsilon_{r,m}}$. The first root in the point spectrum is crucial since it is the only propagating mode in the subwavelength MIMW. (ii) Once a first root is found in the point spectrum, next roots can be found one by one by gradually decreasing the trial root x from the first root. If all of the finite number of roots in the real-axis are found, the next roots are followed by purely imaginary values in the imaginary-axis. This is the procedure of solving all approximate roots in the point spectrum taking into account the real part of $\varepsilon_{r,m}$ only. (iii) Next, we can iteratively approach from the approximate roots to the exact roots by gradually increasing the imaginary part of $\varepsilon_{r,m}$ to the original value in Table 1. In this way, the Muller's method can be applied optimally to this dispersion equation.

3.2 Analysis depending on frequencies

The period and the gap width are determined to be $5\lambda_0$ and $0.1\lambda_0$, respectively. Other examples with different periods and gap widths can be applied, but the physical meaning is not so different. Fig. 2(a) shows the first 20 roots of the point spectrum for four different frequencies using the aforementioned root finding scheme. The filled markers indicate the first roots at each frequency, which are relatively close to the $\sqrt{|\Re\mathrm{e}(\varepsilon_{r,m})|}$ as we mentioned. Following roots are placed one by one as the $\Re\mathrm{e}(\kappa_{m,n}/k_0)$ decreases. Fig. 2(b) shows the typical example of obtaining the first six roots in the case of 100 THz. First, we can obtain the roots with blue squares when the relative permittivity of aluminum is assumed to $\varepsilon_{r,m}$ = –845.11. The first root is 29.090, which is close to $\sqrt{|\Re\mathrm{e}(\varepsilon_{r,m})|}$. The second root of 27.319 and the third root of 21.125 are smaller than the first root. Then the purely imaginary roots j7.341, j27.453, and j40.673 are also easily obtained. Next, by gradually increasing the imaginary part of the $\varepsilon_{r,m}$, we can approach the exact roots as described with green squares using the Muller's method. Note that exact roots are away from the real and imaginary axes, and the travel distances from the axes depend on the magnitude of the imaginary values. Since the imaginary value 3670.2 in $\varepsilon_{r,m}$ at 30 THz is greater than 42.987 at 200 THz, the roots at 30 THz move farther from axes than those at 200 THz, as shown in Fig. 2(a) (For the relative permittivity values, see Table 1). If we do not follow this procedure and put an arbitrary initial trial root in the Muller's method, then the resulting roots do not converge easily to the exact solutions.

The DCS is obtained at the periodic MIMW as discussed in subsection 2.4, and their propagation constants have little effect on wave propagation due to the large attenuation. However, the DCS is important since it contributes to the completeness property of the set of

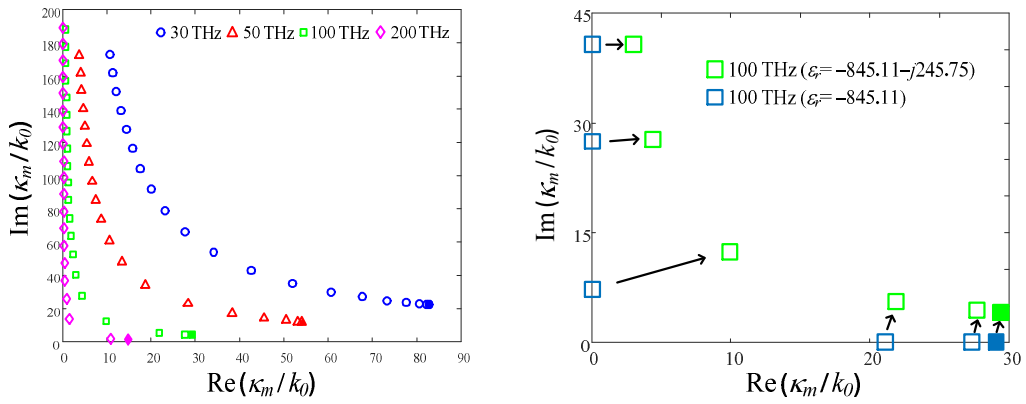

(a) (b)

Fig. 2. (a) First twenty roots κ_m/k_0 in the point spectrum in accordance with the four frequencies in the case of the gap width $2g = 0.1\lambda_0$ and the period $2(g+h) = 5\lambda_0$. (b) The first six roots for considering only real part (blue) and for considering both real and imaginary parts (green) at 100 THz

modes [4]. It is also appropriate to deal with the DCS rather than the continuous spectrum in this paper because the continuous spectrum in non-periodic MIMW is not easy to apply MMT, which will be addressed in Section 4.

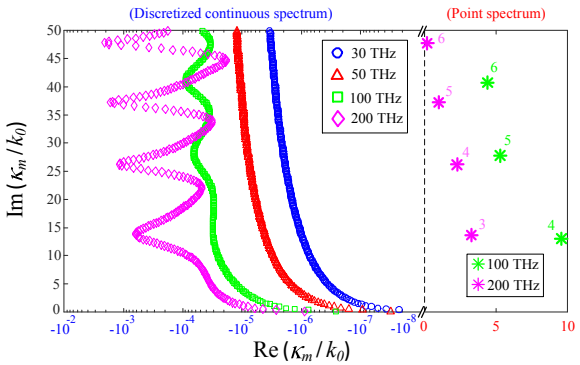

Fig. 3. Roots κ_m/k_0 in the DCS in accordance with the four different frequencies ($2g = 0.1\lambda_0$ and $2(g+h) = 5\lambda_0$). The roots in the point spectrum (three green and four magenta markers) are plotted to emphasize the anti-crossing behavior in the DCS

The left four traces in Fig. 3 show the DCS at four different frequencies. Considering only $\Re\mathrm{e}(\varepsilon_{r,m})$, the roots of the DCS are on the imaginary axis. However, after inserting $\Im\mathrm{m}(\varepsilon_{r,m})$ into Eq. (2), the distributions of DCS are placed away from the imaginary axis (dashed line). The lowest eigenvalue in magnitude $|\kappa_m/k_0|$ at each frequency is the first root of the DCS and represents the lowest harmonics in the metal region. As the $|\kappa_m/k_0|$ increases, higher sinusoidal harmonics are resided in the metal region.

Note that the distributions of DCS at 30 and 50 THz show the monotonic increases as the mode indices are raised. But, the distributions of DCS at 100 and 200 THz fluctuate more than those at 30 and 50 THz, and this phenomenon is called anti-crossing behavior [4]. This phenomenon can be explained by observing the distributions of aforementioned point spectrum in the right side of Fig. 3. For example, the modal eigenvalues at 100 THz with indices of 4, 5, and 6 green markers have a repulsion effect on the DCS distribution, resulting in slight fluctuations of the DCS along the imaginary axis. (4, 5, and 6 mean the 4th, 5th and 6th eigenvalues in the point spectrum at 100 THz.) The DCS distribution at 200 THz is more influenced by the

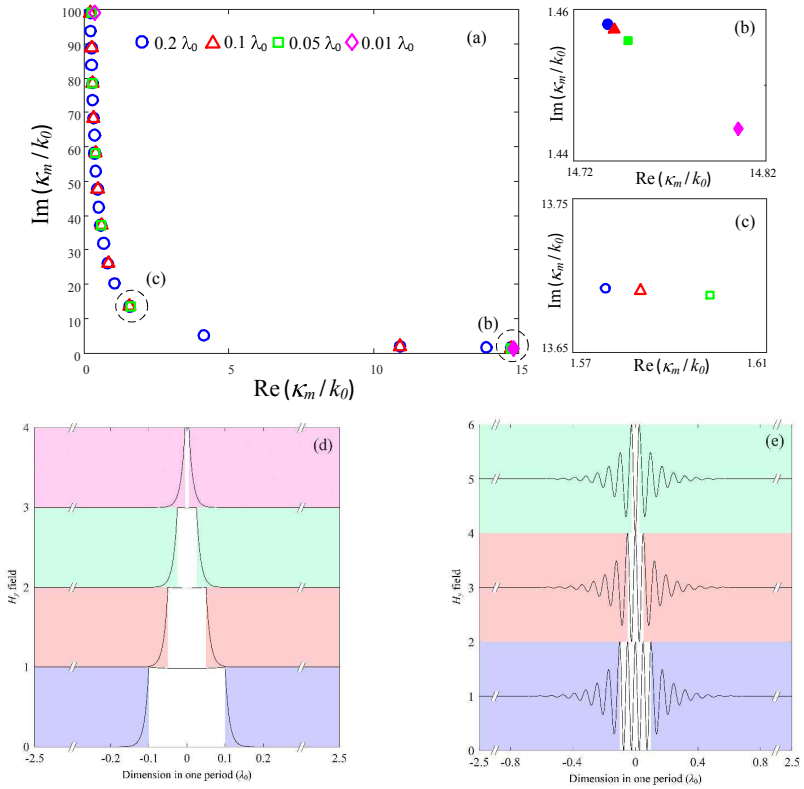

Fig. 4 (a) Roots κ_m/k_0 of the point spectrum with four different gap widths at 200 THz (the period $2(g+h) = 5\lambda_0$). (b) Enlarged view of the first roots near $\kappa_m/k_0 = 14.8 + j1.45$ for four different gap widths. (c) Enlarged view of the roots near $1.59 + j13.7$ for the three different gap widths. (d) H_y-field patterns for the case of (b). Each colored root of (b) corresponds to the field pattern of the same color. The central white region is the part with the insulator. The other regions outside the insulator are Al. Each pattern is shifted by +1 with respect to the previous one for better visualization. (e) H_y-field patterns for the case of (c). Each colored root of (c) corresponds to the field pattern of the same color. The central white region is the part with the insulator. The other regions outside the insulator are Al. Each pattern in green, red, and blue is shifted by +5, +3, and +1, respectively for better visualization

point spectrum, resulting in greater fluctuations since the eigenvalues of the point spectrum with four magenta markers are closer to the imaginary axis than those by 100 THz. This behavior can be understood that each periodically formed field by the mode in the periodic MIMW has a particular effect on the fields of DCS modes, since this phenomenon disappears in a non-periodic MIMW [4]. From another point of view, it is natural effort to maintain orthogonal properties inherent in Eq. (2), although it is not perfect. If we investigate the orthogonal properties by assuming no fluctuations (with no repulsion effect), the orthogonality is slightly dissatisfied.

3.3 Analysis depending on gap widths

In this subsection, we investigate the distributions of the point spectrum and the DCS as a function of the gap width of $0.2\lambda_0$, $0.1\lambda_0$, $0.05\lambda_0$, and $0.01\lambda_0$. These gap widths fall within the subwavelength slit category. In addition, some H_y-field patterns of the point spectrum in accordance with the gap widths are tested. The frequency of interest is 200 THz, and the period of the MIMW is fixed to $5\lambda_0$.

Fig. 4(a) shows the distributions of the point spectrum as a function of four different gap widths. The filled markers represent the first roots of each gap width and almost overlap despite the different gap widths. Fig. 4(b) shows an enlarged view of only first eigenvalues, and now they are shown separately. How to obtain the first roots is already introduced in subsection 3.1, and these are more sensitive than the others in setting up the trial roots for the Muller's method. The point spectrum represents the sinusoidal harmonics in the insulator as the DCS does in the metal, as stated earlier. Fig. 4(d) describes the H_y-field patterns for the first roots of the four different gap widths in Fig. 4(b). The H_y-field patterns are almost flat in the insulator, which are very similar to the pattern of TEM mode in PPW. These are the only propagating modes for each case due to the subwavelength slit geometry and play an important role in the resonant transmission through the subwavelength slit, as will be mentioned in Section 4. Fig. 4(c) is an enlarged view of other roots distribution in the vicinity of $\kappa_m/k_0 \approx 1.59 + j13.7$. The H_y-field patterns in the gap (insulator) for the eigenvalues in Fig. 4(c) are also depicted in the Fig. 4(e). The different sinusoidal harmonics for the three different gap widths are clearly observed. Although the number of zero crossings of the harmonics in the insulator are different, three field patterns have the same peak-to-peak intervals in the gap. The field patterns in the gap can also be expected by the locations of κ_m/k_0 in the point spectrum since the sinusoidal harmonics of the H_y-field are closely related to the values κ_m/k_0. For instance, the number of roots for $2g = 0.01\lambda_0$ is two while it is twenty-one when $2g = 0.2\lambda_0$, as shown in Fig. 4(a). This relation can be expressed as follows:

$$(N_q - 1) : q = (N_{0.01} - 1) : 0.01, \quad \text{where } q = 0.05,\ 0.1, \text{ and } 0.2. \tag{6}$$

N_q is the number of roots when $2g = q\lambda_0$. In other words, when $2g = 0.2\lambda_0$, the interval of the sinusoidal harmonics by the 21st mode is the same as that by the 2nd mode when $2g = 0.01\lambda_0$.

Fig. 5 shows the distributions of the DCS as a function of gap widths and is plotted in a similar manner to Fig. 3. The left traces are for the DCS, and the right markers are for the point spectrum, which are introduced to refer only to the anti-crossing behavior. When $2g = 0.2\lambda_0$, the blue distribution moves away from the imaginary axis and exhibits fluctuations by the markers 4, 5, 6, and 7 in the point spectrum. As already introduced in subsection 3.1 as the anti-crossing behavior, the distribution of the DCS further recedes from the imaginary axis when the blue markers approach the imaginary axis. The closer the roots are to the imaginary axis in the point spectrum, the more the repulsion effect on the DCS distribution is observed. A similar effect is also observed when $2g = 0.1\lambda_0$ and $0.05\lambda_0$.

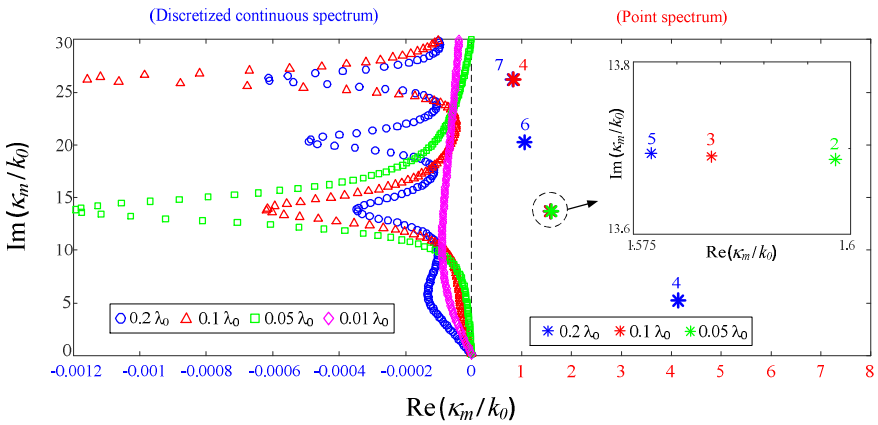

Fig. 5 Roots in κ_m/k_0 of the DCS with four different gap widths at 200 THz ($2(g+h) = 5\lambda_0$). The higher eigenvalues ($\Im\mathrm{m}(\kappa_m/k_0) > 30$) are excluded. The point spectrum on the right is plotted to emphasize the anti-crossing behavior. An inset figure is included to expand the superimposed roots of the point spectrum

For instance, the fourth red root (≈ 0.84 + *j*26.2) repels the DCS distribution more than the third red root (≈ 1.58 + *j*13.7). Another noteworthy feature in the anti-crossing behavior is found at the roots near 1.58 + *j*13.7, which are nearly superimposed and distinguishable in the enlarged inset of Fig. 5. Even if the values of three roots in the inset are nearly the same, the repulsion effects are quite different. To be precise, the blue DCS distribution is less repelled, although the 5th blue marker is slightly closer to the imaginary axis. This unexpected and odd repulsion is not enough to be explained by the anti-crossing behavior alone. It can be better understood by the H_y-field patterns in Fig. 4(e), where the roots in the inset of Fig. 5 are the same as the roots in Fig. 4(c). As stated previously, the distributions of the DCS have fluctuations from the repulsion effect to satisfy the orthogonality. Although the markers of the point spectrum are placed almost at the same location, the strengths of the repulsion effect are different depending on the mode order of the H_y-field patterns. The lower the mode order, the stronger the repulsion effect. For instance, the field pattern of the 2nd green root in the inset of Fig. 5 is described at the top of Fig. 4(e). The H_y-field of the root stands for the TM_2 mode, in which two zero crossings are observed in the insulator. On the other hand, the field pattern of the 5th blue root in the inset of Fig. 5 is shown at the bottom of the Fig. 4(e). The H_y-field of the root represents the TM_8 mode since the number of zero crossings is 8 in the insulator. As the mode number of sinusoidal harmonics in the insulator decreases, the distribution of the DCS exhibits stronger repulsion effect as observed at near *j*13.7, although eigenvalues in the point spectrum are nearly the same.

3.4 Analysis depending on periods

Fig. 6 illustrates the point spectrum and the DCS according to the periods $5\lambda_0$, $10\lambda_0$, $15\lambda_0$ and $20\lambda_0$ when the gap width $2g = 0.1\lambda_0$, and the frequency of interest is 200 THz. The markers of the point spectrum are rarely shifted with the variation of period since the sinusoidal harmonics of the H_y-field in the insulator also do not change regardless of the variation in the period. Therefore, just the 3rd and 4th roots in the point spectrum are plotted to emphasize the anti-crossing behavior.

The distributions of the DCS are shown in the negative real part of κ_m/k_0 in Fig. 6. Each root describes the sinusoidal harmonics of H_y-field primarily in the metal. Because the metal portion is much wider than the insulator within a single period, the wide period allows to reside in more sinusoidal harmonics in the metal. So the number of roots in the range $\Im\mathrm{m}(\kappa_m/k_0) = (0, 30)$ with a period $20\lambda_0$ is 327 while the number is 154 with a period $5\lambda_0$ in the same range. The use of more harmonics has the advantage of accurately solving electromagnetic scattering or diffraction problems through a single subwavelength slit. For more discussions, see the appendix in [7]. Furthermore, we can

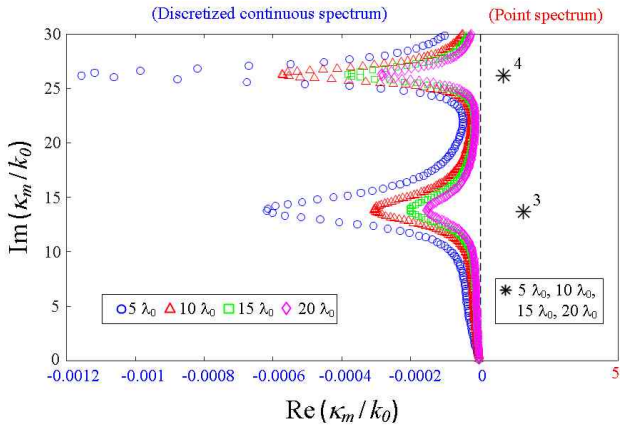

Fig. 6. Roots κ_m/k_0 in the DCS with four different periods at 200 THz ($2g = 0.1\lambda_0$). The eigenvalues in the point spectrum, noted as black 3 and 4, at the right side are shown overlapping for four different periods. The wider the period, the denser the eigenvalues in the DCS and less anti-crossing behavior

find the different anti-crossing behaviors for different periods. As shown in the Fig. 6, when the period = $5\lambda_0$, the distribution of the DCS is more receded than that by $20\lambda_0$. It can be understood that all modes with a small period give close effects to each other, while the effects are getting smaller as the period increases. In other words, the modes are highly coupled with a small period, whereas the coupling of the modes gradually decreases as the period is enlarged, and eventually the modes are not coupled at all for an infinite period, which is a non-periodic slit.

Scattering or diffraction of a single subwavelength slit can be solved directly by some techniques, and it can be also solved by transition from a periodic MIMW to a single subwavelength slit. In the latter case, a wide periodic MIMW can better imitate a single subwavelength slit. Therefore, the MIMW with a wide period is preferable to solve the diffraction and transmission of a single subwavelength slit. However, the wider period involves a larger number of modes, resulting in increased elements in the matrix calculation, which eventually results in much more computation time. Therefore, choosing a proper period is one of the important criteria for the single subwavelength slit problem. In the following section, we set the period for the slit problem to $5\lambda_0$ since the period $5\lambda_0$ is enough to include sufficient modes and thus nearly close to the original problem.

4. Transmittance

Now, we investigate the transmittances through a single subwavelength slit of PEC and real metal plates. The periodic MIMW in Fig. 1 can be extended to the geometry of a single subwavelength silt in Fig. 7 by assuming a finite thickness *d* in the *z*-direction and setting *x*-

direction as non- periodic (infinite to $+x$ and $-x$ directions). We focused on the thickness d in this geometry to investigate the resonance phenomenon in the transmission through the slit, while Fig. 1 examines the *guiding* structure in an infinite z-direction. An electromagnetic plane wave is normally incident from the left free space and transmitted into the right free space. As is usual for this geometry, only TM polarization is focused on. The transmittance τ (dimensionless) is defined as [23]

$$\tau = \frac{1}{2g}\frac{P_t}{W_i} = \frac{1}{4gW_i}\int_L \Re\mathfrak{e}\left[\vec{E}\times\vec{H}^*\right]\cdot\hat{z}dS\,, \tag{7}$$

where P_t is the transmitted power into the right free space, and W_i is the incident power density in the left free space. The line integration is carried out over the L, the boundary between the slit and the right free space. The MMT is applied to obtain the transmittances through the subwavelength slit of Fig. 7, but the transmittance of the non-periodic MIMW along x-directions is not easily obtained by the MMT. Thus, we adopt the structure in Fig. 1 as an intermediate stage and gradually extend the period until it approaches a wider-periodic geometry with the transmittance close to the subwavelength slit of Fig. 7. The convergence of the transmittances is observed in [7], and the detailed procedures including MMT equations and multi-junction problem are introduced in [7, 24, 25].

Based on the studies of point spectrum and DCS in Section 3, transmittances through a metallic subwavelength silt can be observed. The more detailed process to obtain the transmittances is dealt with in [7]. In this work, we observe and compare the transmittances through Ag, Al, and Cu. The transmittances as functions of frequency, metal, and plate thickness are shown in Fig. 8 with the constant gap width $2g=0.05\lambda_0$. The transmitted power through the slit into the right free space can be calculated as $P_t = W_i \times \tau \times 2g$. For example, the repeated peak values

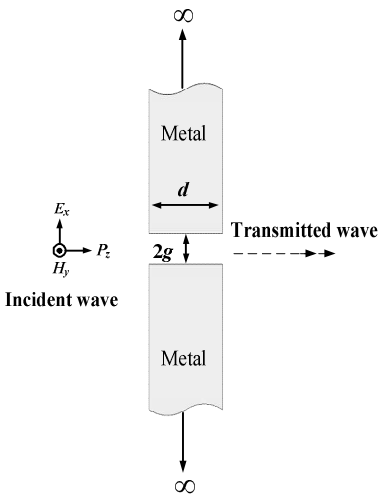

Fig. 7. Geometry of a single subwavelength slit in the non-periodic MIMW. A normal and TM-polarized electromagnetic wave is incident from the left free space and transmitted into the right free space. The plate thickness d is variable, and the gap width $2g$ is constant as $0.05\lambda_0$

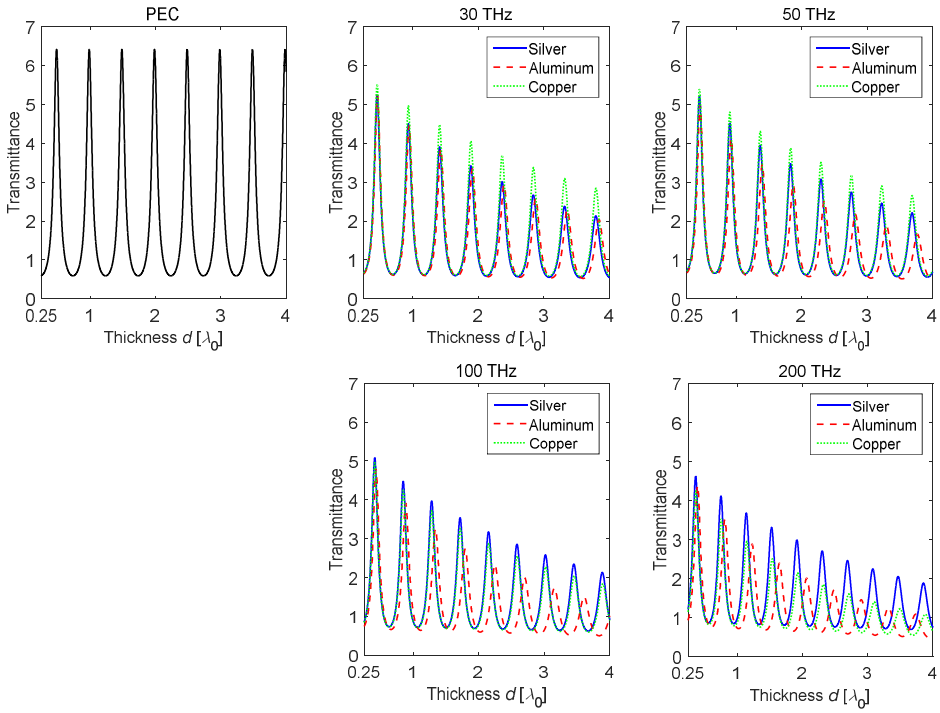

Fig. 8. Transmittances versus the plate thickness d with $2g = 0.05\lambda_0$ for the structure in Fig. 7. Ag, Al, and Cu at four frequencies are tested

in the PEC are equally observed as 6.366. Then, the transmitted power P_t of $6.366 \times 0.05\lambda_0$ (When $W_i = 1$ W/m) at the repeated peaks is delivered into the opposite region. On the other hand, the lowest transmittance is observed to be less than 1, which means that incidence power density residing in an area smaller than the gap width can be transmitted through the slit. This periodic transmittance is understood as the resonance phenomenon [23, 26-30].

Crucial features in Fig. 8 are as follows. (i) The transmittance patterns at low frequencies similarly follow those of the PEC, while the patterns at higher frequencies begin to differ from the PEC. At lower frequencies, such as microwave band, real metals can be regarded as PEC, so this trend is expected and understandable. On the other hand, more discrepancies are observed at high frequencies since the large attenuation is embedded in real metals. In addition, the repeated peaks in transmittance are gradually attenuated because the real metals are lossy, and thicker plates have more ohmic loss. (ii) The intervals of periodic peaks in transmittances of the PEC are comparable with those of other metals. The equal peaks in the PEC appear repeatedly with an interval of $0.5\lambda_0$. Meanwhile, the intervals of repeated peaks for real metals are similar, but slightly different and less than $0.5\lambda_0$. This is caused by the fact that the propagation constants $k_{z,0}$ of the dominant propagating mode for real metals are slightly larger than those for PEC. The appearance of periodic peaks of Ag and Cu are similar despite the different attenuations, while the intervals of periodic peaks of Al is slightly greater than those of Ag and Cu due to the smaller propagation constants of Al. (iii) It is interesting to note that the minimum transmittances for the metals at 100 and 200 THz are *larger* than those for the PEC when the thickness d is relatively thin. This is because the power transmission at thinner metal plate includes the high-order modes as well as the dominant propagating mode, while the transmission in PEC includes the only dominant propagating mode at all plate thicknesses. (iv) The transmittance tendencies for the Ag and Cu are similar but dissimilar from Al. This can be understandable from the material properties in Table 1 where Ag and Cu are comparable, but Al is somewhat distinctive. Another remarkable point between Ag and Cu is that the Cu has a lower loss at 30 and 50 THz than Ag, but unusually has a greater loss at 200 THz than Ag due to the unique relative permittivity of Cu in Table 1.

5. Conclusion

In this paper, we analyzed the eigenvalue distributions as functions of frequencies, gap widths, and periods for the periodic MIMW with aluminum. The Muller's method was applied to solve the eigenvalues for the dispersion equation, which is the most fundamental equation in the MIMW. To efficiently solve the exact roots of the eigenvalues, we used the scheme for finding proper initial values of the dispersion equation by considering only $\Re e(\varepsilon_{r,m})$, and the exact roots can be iteratively found by increasing $|\Im m(\varepsilon_{r,m})|$ in the Muller's method. The results showed that the first roots of the point spectrum at each frequency are relatively close to the $\sqrt{|\Re e(\varepsilon_{r,m})|}$. The anti-crossing behavior was observed that the distribution of the DCS further receded from the imaginary axis when the point spectrum approached the imaginary axis. This behavior became stronger for the low-order modes in the point spectrum and weaker as the period of the MIMW was increased, while the point spectrum was rarely shifted depending on the period.

In addition, we obtained the transmittances through a single slit for PEC and real metal plates. The transmittance patterns in real metals at low frequencies similarly followed those of the PEC, while the patterns at higher frequencies began to differ from the PEC. The intervals of periodic peaks in transmittances of the real metals were slightly shorter than those of the PEC because the dominant propagation constant for real metals is slightly larger than that for PEC. Especially, the transmittances of Cu had lower loss at 30 and 50 THz than those of Ag, but had more loss at 200 THz than Ag due to the unique relative permittivity of Cu. The current transmission analysis can be extended for the problems of the multiple slit cases or layered media.

Acknowledgements

This work was partly supported by ICT R&D program of MSIP/IITP 2016-0-00130 and Basic Science Research Program through the National Research Foundation of Korea(NRF) funded by the Ministry of Education (Nos. 2013R1A6A3A03022194 and 2015R1A6A1A03031833).

References

[1] B. Sturman, E. Podivilov, and M. Gorkunov, "Eigenmodes for metal-dielectric light-transmitting nanostructures," *Physical Review B*, vol. 76, no. 12, pp. 125104(11), Sept. 2007.

[2] B. Sturman, E. Podivilov, and M. Gorkunov, "Eigenmodes for the problem of extraordinary light transmission through subwavelength holes," *EPL*, vol. 80, no. 2, pp. 24002(5), Oct. 2007.

[3] B. Sturman, E. Podivilov, and M. Gorkunov, "Theory of extraordinary light transmission through arrays of subwavelength slits," *Physical Review B*, vol. 77, no. 7, pp. 075106(12), Feb. 2008.

[4] S. E. Kocabas, G. Veronis, D. A. B. Miller, and S. Fan, "Modal analysis and coupling in metal-insulator-metal waveguides," *Physical Review B*, vol. 79, no. 3,

pp. 035120(17), Jan. 2009.
[5] M. Gorkunov, E. Podivilov, and B. Sturman, "Transmission and scattering properties of subwavelength slits in metals," *Physical Review B*, vol. 83, no. 3, pp. 035414(11), Jan. 2011.
[6] B. Sturman, E. Podivilov, and M. Gorkunov, "Elementary processes of light transformation for slit structures in real and perfect metals," *Photonics and Nanostructures - Fundamentals and Applications*, vol. 10, no. 4, pp. 409-415, Oct. 2012.
[7] J.-E. Park, F. L. Teixeira, and B.-H. V. Borges, "Analysis of deep-subwavelength Au and Ag slit transmittances at terahertz frequencies," *Journal of the Optical Society of America B*, vol. 33, no. 7, pp. 1355-1364, Jul. 2016.
[8] C. F. Bohren and D. R. Huffman, "Absorption and scattering of light by small particles," *Wiley, New York*, 1983.
[9] J. Won, S. Jeon, and S. Nam, "Identifying the appropriate position on the ground plane for MIMO antennas using characteristic mode analysis," *J Electromagn Eng Sci*, vol. 16, no. 2, pp. 119-125, Apr. 2016.
[10] N. Zhang and W. Nah, "Mode analysis of cascaded four-conductor lines using extended mixed-mode S-Parameters," *J Electromagn Eng Sci*, vol. 16, no. 1, pp. 57-65, Jan. 2016.
[11] E. Kreyszig, "Introductory functional analysis with applications," *Wiley, New York*, 1978.
[12] J. Locker, "Spectral theory of non-self-adjoint two-point differential operators," *American Mathematical Society, Providence*, 2000.
[13] K. E. Atkinson, "An introduction to numerical analysis," *Wiley*, 1989.
[14] G. Veronis, Z. Yu, S. E. Kocabas, D. A. B. Miller, M. L. Brongersma, and S. Fan, "Metal-dielectric-metal plasmonic waveguide devices for manipulating light at the nanoscale," *Chinese Optics Letters*, vol. 7, no. 4, pp. 302-308, Apr. 2009.
[15] G. Wang, H. Lu, X. Liu, D. Mao, and L. Duan, "Tunable multi-channel wavelength demultiplexer based on MIM plasmonic nanodisk resonators at telecommunications regime," *Optics Express*, vol. 19, no. 4, pp. 3513-3518, Feb. 2011.
[16] P. Sheng, R. S. Stepleman, and P. N. Sanda, "Exact eigenfunctions for square-wave gratings: Application to diffraction and surface-plasmon calculations," *Physical Review B*, vol. 26, no. 6, pp. 2907-2916, Sept. 1982.
[17] E. Feigenbaum and M. Orenstein, "Modeling of complementary (void) plasmon waveguiding", *Journal of Lightwave Technology*, vol. 25, no. 9, pp. 2547-2562, Sept. 2007.
[18] A. D. Rakic, A. B. Djurisic, J. M. Elazar, and M. L. Majewski, "Optical properties of metallic films for vertical-cavity optoelectronic devices," *Applied Optics*, vol. 37, no. 22, pp. 5271-5283, Aug. 1998.
[19] E. Anemogiannis and E. N. Glytsis, "Multilayer waveguide: Efficient numerical analysis of general structures," *Journal of Lightwave Technology*, vol. 10, no. 10, pp. 1344-1351, Oct. 1992.
[20] R. E. Smith, S. N. Houde-Walter, and G. W. Forbes, "Mode determination for planar waveguides using the four-sheeted dispersion relation," *IEEE Journal of Quantum Electronics*, vol. 28, no. 6, pp. 1520-1526, Jun. 1992.
[21] Min-Suk Kwon and Sang-Yung Shin, "Simple and fast numerical analysis of multilayer waveguide modes," *Optics Communications*, vol. 233, no. 1, pp. 119-126, Mar. 2004.
[22] R. Rodríguez-Berral, F. Mesa, and F. Medina, "Appropriate formulation of the characteristic equation for open nonreciprocal layered waveguides with different upper and lower half-spaces," *IEEE Transactions on microwave theory and techniques*, vol. 53, no. 5, pp. 1613-1623, May 2005.
[23] R. F. Harrington and D. T. Auckland, "Electromagnetic transmission through narrow slots in thick conducting screens," *IEEE Transactions on Antennas and Propagation*, vol. 28, no. 5, pp. 616-622, Sept. 1980.
[24] A. Wexler, "Solution of waveguide discontinuities by modal analysis," *IEEE Transactions on Microwave Theory and Techniques*, vol. 15, no. 9, pp. 508-517, Sept. 1967.
[25] W. C. Chew, "Waves and Fields in Inhomogeneous Media," *Wiley-IEEE*, 1999.
[26] Y. Takakura, "Optical resonance in a narrow slit in a thick metallic screen," *Physical Review Letters*, vol. 86, no. 24, pp. 5601-5603, Jun. 2001.
[27] F. Yang and J. R. Sambles, "Resonant transmission of microwaves through a narrow metallic slit," *Physical Review Letters*, vol. 89, no. 6, pp. 063901(3), Jul. 2002.
[28] J. Bravo-Abad, L. Martín-Moreno, and F. J. García-Vidal, "Transmission properties of a single metallic slit: From the subwavelength regime to the geometrical-optics limit," *Physical Review E*, vol. 69, no. 2, pp. 026601(6), Feb. 2004.
[29] F. J. García-Vidal, E. Moreno, J. A. Porto, and L. Martín-Moreno, "Transmission of light through a single rectangular hole," *Physical Review Letters*, vol. 95, no. 10, pp. 103901(4), Aug. 2005.
[30] J. -E. Park, K. Y. Kim, and J. -W. Song, "Comparison of mutual coupling phenomena in subwavelength ridged circular apertures and half-wavelength dipole antenna arrays," *International journal of antennas and propagation*, vol. 2012, pp. 129469(8), Dec. 2012.

Jun Hur received the B.S. and M.S. degrees in electronic and electrical engineering from Hongik University, Seoul, Korea, in 2014 and 2016, respectively. He is currently working toward the Ph.D. degree in electronics and computer engineering at Hongik University, Seoul, Korea. His research interests include the global positioning system antennas, antenna arrays, and position optimization of array elements for adaptive beamforming.

Hosung Choo received the B.S. degree in radio science and engineering from Hanyang University in Seoul in 1998, and the M.S. and Ph.D. degrees in electrical and computer engineering from the University of Texas at Austin, in 2000 and 2003, respectively. In September 2003, he joined the school of electronic and electrical engineering, Hongik University, Seoul, Korea, where he is currently a full professor. His principal areas of research are the use of the optimization algorithm in developing antennas and microwave absorbers. His studies include the design of small antennas for wireless communications, reader and tag antennas for RFID, and on-glass and conformal antennas for vehicles and aircraft.

Jong-Eon Park received the B.S., M. S., and Ph. D. degrees in School of Electrical Engineering and Computer Science from Kyungpook National University, Daegu, Korea, in 2006, 2009, and 2013, respectively. From 2013 to 2015, he was a post-doctoral researcher with the Ohio State University. Since 2016, he has been with Hongik University, where he is currently a research professor in the Metamaterial Electronic Device Research Center. His research interests include scattering through aperture, antenna design, computational electromagnetics, etc.